Magnetization, phonon, and X-ray edge absorption in barium doped BiFeO3 ceramics

Authors: Yi Ting, Chi-Shun Tu, Pin-Yi Chen, Cheng-Sao Chen, J. Anthoniappen, V. Hugo Schmidt, Jenn-Min Lee, Ting-Shan Chan, Wei-Yu Chen, and Rui-Wen Song

The final publication is available at Springer via http://dx.doi.org/10.1007/s10853-016-0355-0.

Ting, Yi, Chi-Shun Tu, Pin-Yi Chen, Cheng-Sao Chen, J Anthoniappen, V Hugo Schmidt, Jenn-Min Lee, Ting-Shan Chan, Wei-Yu Chen, and Rui-Wen Song. "Magnetization, phonon, and X-ray edge absorption in barium doped BiFeO3 ceramics." Journal of Material Science 52, no. 1 (January 2017): 581-594. DOI:https://dx.doi.org/10.1007/s10853-016-0355-0.

Magnetization, phonon, and X-ray edge absorption in barium-doped $BiFeO_3$ ceramics

Yi Ting[1], Chi-Shun Tu[1,*], Pin-Yi Chen[2], Cheng-Sao Chen[3], J. Anthoniappen[4], V. H. Schmidt[5], Jenn-Min Lee[6], Ting-Shan Chan[6], Wei-Yu Chen[7], and Rui-Wen Song[7]

[1] *Department of Physics, Fu Jen Catholic University, New Taipei City 24205, Taiwan*
[2] *Department of Mechanical Engineering, Ming Chi University of Technology, New Taipei City 24301, Taiwan*
[3] *Department of Mechanical Engineering, Hwa Hsia University of Technology, New Taipei City 23567, Taiwan*
[4] *Department of Physics, University of San Carlos, 6000 Cebu City, Philippines*
[5] *Department of Physics, Montana State University, Bozeman, MT 59717, USA*
[6] *National Synchrotron Radiation Research Center, Hsinchu 30076, Taiwan*
[7] *Department of Materials Science and Engineering, National Tsing Hua University, Hsinchu, Taiwan*

ABSTRACT

Magnetization hysteresis loops, dc and ac magnetic susceptibilities, and Raman vibrations have been characterized in $(Bi_{1-x}Ba_x)FeO_{3-\delta}$ ceramics for $x = 0.0$, 0.05, 0.10, and 0.15 as functions of temperature. Ferromagnetic hysteresis loops were observed in Ba-doped compounds with increasing magnetization as Ba substitution increases. High-resolution synchrotron Fe *K*- and $L_{2,3}$-edge X-ray absorptions reveal an Fe^{3+} valence and a modification of the Fe–O–Fe bond structure by the A-site Ba substitution. The oxygen *K*-edge X-ray absorption suggests that the hybridization of the O 2*p* and Fe 3*d* orbitals was reduced by the Ba^{2+} substitution. Field-cooled and zero-field-cooled magnetic susceptibilities reveal a spin-glass behavior, which was enhanced with increasing Ba substitution. Raman vibrations of the Bi- and Fe-sensitive $E(2)$ and $A_1(1)$ modes reveal frequency softening and step-like anomalies in full-width-at-half-maximum in the vicinity of $\sim$150–250 K, which were attributed to spin–phonon interaction while magnetic ordering transitions take place.

Introduction

Phonon studies of perovskite bismuth ferrite $BiFeO_3$ (BFO) have demonstrated that the coupling effects between low-lying spin-wave excitations (or magnons) and optical phonons gave promising spin-wave-based spintronic applications [1, 2]. $BiFeO_3$ is one of the most studied multiferroic materials because of its high Néel temperature ($T_N \sim 640$ K) and Curie temperature ($T_C \sim 1100$ K) [3]. The hybridization of Bi 6*p* and O 2*p* orbital configurations in $BiFeO_3$ causes an off-center displacement of the Bi^{3+} ion to cause ferroelectricity [4]. The Fe^{3+} spin orientation in $BiFeO_3$ displays a G-type canted

antiferromagnetic ordering with a cycloidal incommensurate periodicity of $\lambda_o \sim 62$ nm [5, 6]. The magnetoelectric interaction between the canted Fe^{3+} spins and the ferroelectric polarization plays an essential role for the cycloidal variation. Neutron diffraction suggested that the modulated cycloidal ordering of the Fe^{3+} magnetic moments in $BiFeO_3$ remains the same from 4 K up to $T_N \sim 640$ K [7].

Linear antiferromagnetic behavior and electric leakage have limited $BiFeO_3$ for electromagnetic applications. A-site substitutions of rare-earth elements onto the $BiFeO_3$ perovskite cell have been employed to enhance ferromagnetic, ferroelectric, and photovoltaic responses [8–11]. A-site substitutions of alkaline earth metal elements in $BiFeO_3$, i.e., $(Bi_{1-x}A_x)FeO_3$ (A = Ca, Sr, Ba), have also demonstrated an improvement of magnetic and ferroelectric properties [12–23]. It was proposed that magnetization can be enhanced as the doping ion radius increases due to suppression of the antiferromagnetic spiral spin configuration in $BiFeO_3$ [23]. The magnetization enhancement in $Bi_{0.8}A_{0.2}FeO_3$ (A = La, Ca, Sr, Ba) ceramics was attributed to the intrinsic structural distortion [22]. It was found that heterovalent substitution of A^{2+} in $BiFeO_3$ caused the formation of oxygen vacancies without the occurrence of Fe^{4+} [22]. X-ray photoelectron spectroscopy (XPS) suggested a reduction of oxygen vacancies in $(Bi_{1-x}Ba_x)FeO_3$ ($0.0 \le x \le 0.25$) ceramics [24]. $(Bi_{1-x}Ba_x)FeO_3$ ($0.0 \le x \le 0.30$) ceramics showed increasing magnetization hysteresis loops with Ba concentration [12, 14]. X-ray diffraction spectra of $(Bi_{1-x}Ba_x)FeO_3$ (x = 0.0–0.25) ceramics revealed a structure shift from rhombohedral to pseudocubic as Ba substitution increases [25]. A rhombohedral–tetragonal structural transition was suggested for $x = 0.35$ at room temperature [14]. Thermal analysis in $(Bi_{1-x}Ba_x)FeO_3$ ($0.0 \le x \le 0.25$) ceramics suggested that ferroelectric and magnetic transitions shift toward higher temperature with increasing Ba concentration [16].

The field-cooled (FC) and zero-field-cooled (ZFC) magnetizations revealed a spin-glass behavior in $BiFeO_3$ below room temperature [26–29]. The origin of spin-glass features is associated with magnetic ordering competition, randomness of magnetic ions, and distorted lattices [30]. The spin-glass phenomenon in $BiFeO_3$ was correlated to a spin-reorientation transition as seen in rare-earth orthoferrites ($RFeO_3$, R = rare-earth element) [31–34]. However, the spin reorientation in orthoferrites was correlated to the magnetic moments of the rare-earth ions [35] and thus may not be applicable for non-magnetic Bi^{3+} ion in $BiFeO_3$ [36]. Temperature-dependent Raman anomalies have been reported in low-lying magnons and phonons in the region of 100–250 K in $BiFeO_3$ crystals [37–40], ceramics [41, 42], and thin films [43–46]. Two types of magnons below 60 cm^{-1} were identified in BFO crystals and correspond to magnetization lying in and out of the cycloid plane, i.e., cyclon (ϕ) and extra-cyclon (ψ) modes [47]. It was suggested that the spin-reorientation transition is responsible for temperature-dependent Raman anomalies [39, 43, 47]. However, neutron diffraction suggested that there is no detectable reorientation of the Fe^{3+} spin moments in BFO crystals below room temperature and that Raman anomalies of low-lying magnon may link to mode freezing [48, 49]. Neutron scattering suggested that temperature-dependent dynamics of low-lying magnons is associated with the easy-axis single-ion anisotropy and Dzyaloshinskii–Moriya interaction, which correlates with the Fe–O–Fe bond angle [50].

Electronic correlation, phonon vibration, and magnetic susceptibility in A-site alkaline earth element-substituted $BiFeO_3$ still lack study below room temperature. This work explores the A-site Ba^{2+} substitution effects on magnetization and Raman-active phonon vibrations in $(Bi_{1-x}Ba_x)FeO_{3-\delta}$ (x = 0.0, 0.05, 0.10, 0.15) ceramics as functions of temperature. High-resolution synchrotron X-ray Fe K-edge, Fe $L_{2,3}$-edge, and oxygen K-edge absorptions were measured to analyze electronic valence, Fe–O–Fe bond structure, and hybridization of the O 2p and the unoccupied Fe 3d orbital states. FC, ZFC, and ac magnetic susceptibilities were measured to study magnetic ordering and the spin-glass behavior.

Experimental procedure

Ceramic preparation

$BiFeO_3$ (BFO), $(Bi_{0.95}Ba_{0.05})FeO_{2.975}$ (BFO5Ba), $(Bi_{0.90}Ba_{0.10})FeO_{2.95}$ (BFO10Ba), and $(Bi_{0.85}Ba_{0.15})FeO_{2.925}$ (BFO15Ba) ceramics were prepared by the solid-state reaction method, in which Bi_2O_3, $BaCO_3$, and Fe_2O_3 powders (purity ≥99.0 %) were weighed in 1.1:0:1.0, 0.95:0.1:1.0, 0.90:0.20:1.0, and 0.85:0.3:1.0 ratios, respectively. The powders were mixed in an agate mortar with alcohol as a medium for more than 24 h.

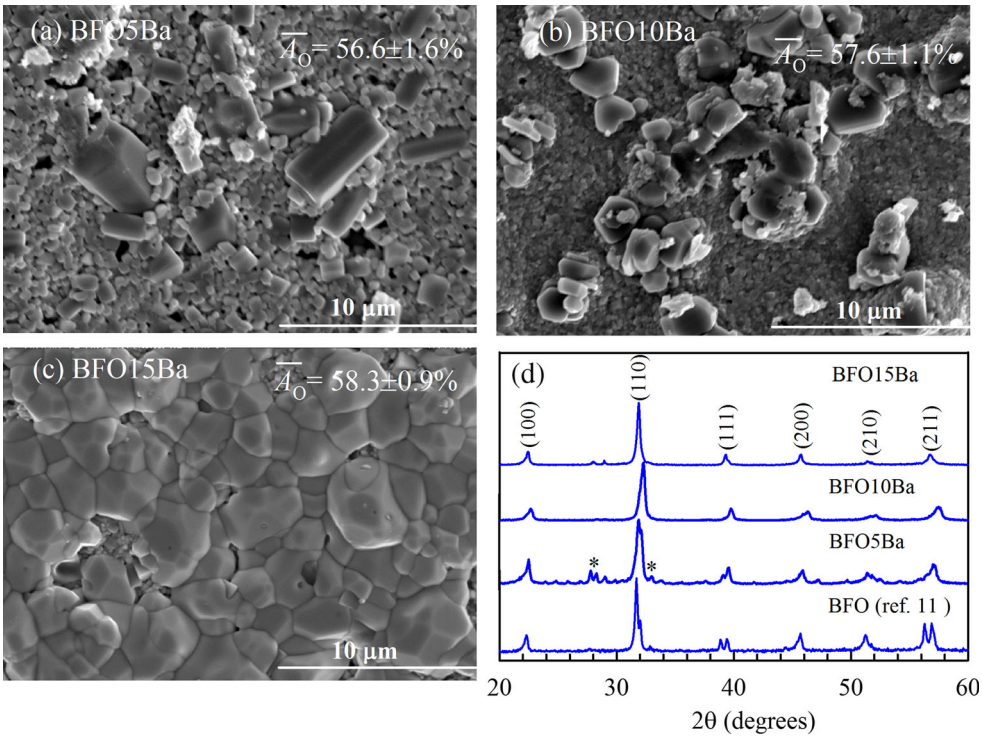

Figure 1 **a**–**c** SEM grain morphologies of thermally etched ceramics and **d** XRD spectra of the as-sintered ceramics at room temperature. $\bar{A}_O$ is the average oxygen atomic ratio.

The dried mixtures were calcined at 800 °C for 3 h. The dried mixtures were calcined at 800 °C (3 h) for all the compounds and then sintered at 830 °C (10 h) for BFO, 845 °C (3 h) for BFO5Ba, and 865 °C (3 h) for both BFO10Ba and BFO15Ba.

Characterization

Grain morphologies and oxygen atomic ratios were characterized using a Hitachi S-3400N scanning electron microscope (SEM) and a JEOL JXA-8500F field emission electron probe microanalyzer (EPMA), respectively. Standard deviations were calculated to estimate error ranges of average oxygen atomic ratios. X-ray diffraction spectra of the as-sintered ceramics were obtained using a Rigaku multiplex diffractometer. A superconducting quantum interface device (SQUID)-based magnetometer (quantum design MPMSXL) was used for the measurements of magnetization hysteresis loops and magnetic susceptibilities. ZFC and FC magnetic susceptibilities (χ_{ZFC} and χ_{FC}) were measured under a dc magnetic field (H = 100 Oe). For ac magnetic susceptibility, an oscillating field of amplitude H = 3 Oe was used without a dc bias magnetic field upon heating. The Fe *K*-edge synchrotron X-ray absorption spectroscopy (XAS) was performed in transmission mode at the 01C1 beam line of the National Synchrotron Radiation Research Center (NSRRC) in Taiwan. The X-ray absorption spectra of the Fe $L_{2,3}$-edges and oxygen *K*-edge were studied in total electron yield via current mode at the 20A1 beam line of the NSRRC. The backscattering Raman spectroscopy was performed using a Nanobase Model XperRam 200 Raman spectrometer equipped with a green laser of $\lambda = 532$ nm. A Linkam THMS600 heating/cooling stage was mounted on the microscope for temperature control.

Results and discussion

Figure 1(a–c) shows grain morphologies of thermally etched BFO5Ba, BFO10Ba, and BFO15Ba ceramics. As shown in Fig. 1(a–c), the average oxygen atomic ratios ($\bar{A}_O$) are about 56.6 ± 1.6, 57.6 ± 1.1, and 58.3 ± 0.9 % for BFO5Ba, BFO10Ba, and BFO15Ba, respectively. The BFO ceramic has a $\bar{A}_O$ ~52.5 ± 1.6 % [11]. The $BiFeO_3$ formula oxygen atomic ratio is 60 %. This suggests that average oxygen vacancies (OVs) decrease with increasing A-site Ba^{2+} substitution. X-ray photoelectron spectroscopy (XPS) also suggested a reduction of OVs in $(Bi_{1-x}Ba_x)FeO_3$ ceramics ($0 \le x \le 0.25$) with increasing Ba^{2+} doping concentration [24]. The formations of OVs and Fe valence shift may be caused by

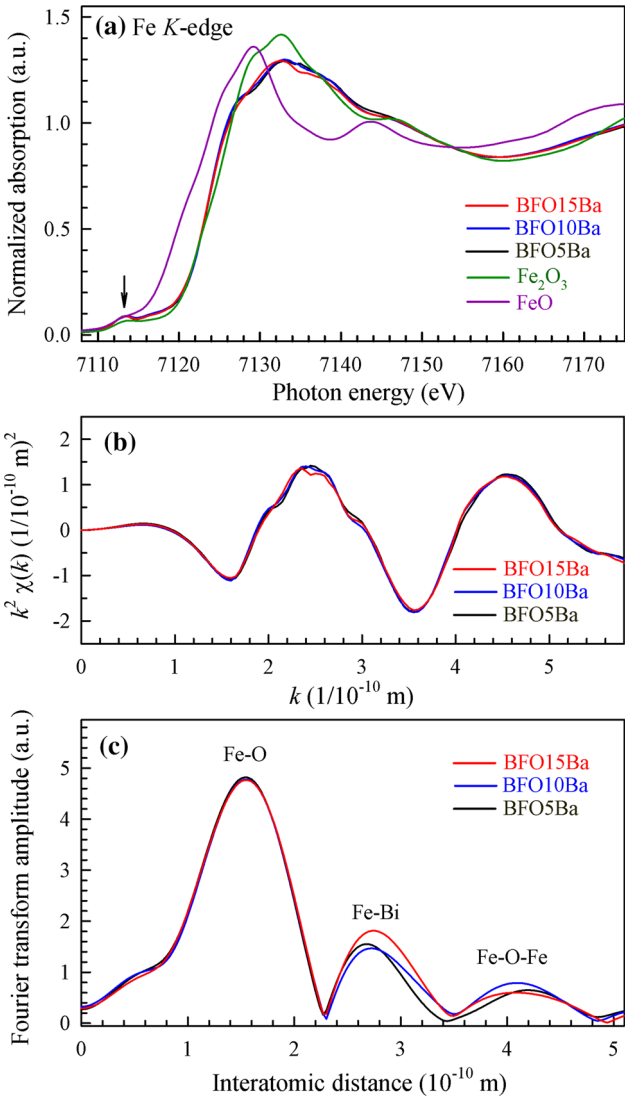

Figure 2 **a** Fe *K*-edge XANES spectra versus photon energy, **b** $k^2\chi(k)$ versus k, and **c** Fourier transform amplitude of $k^2\chi(k)$ versus interatomic distance without phase correction.

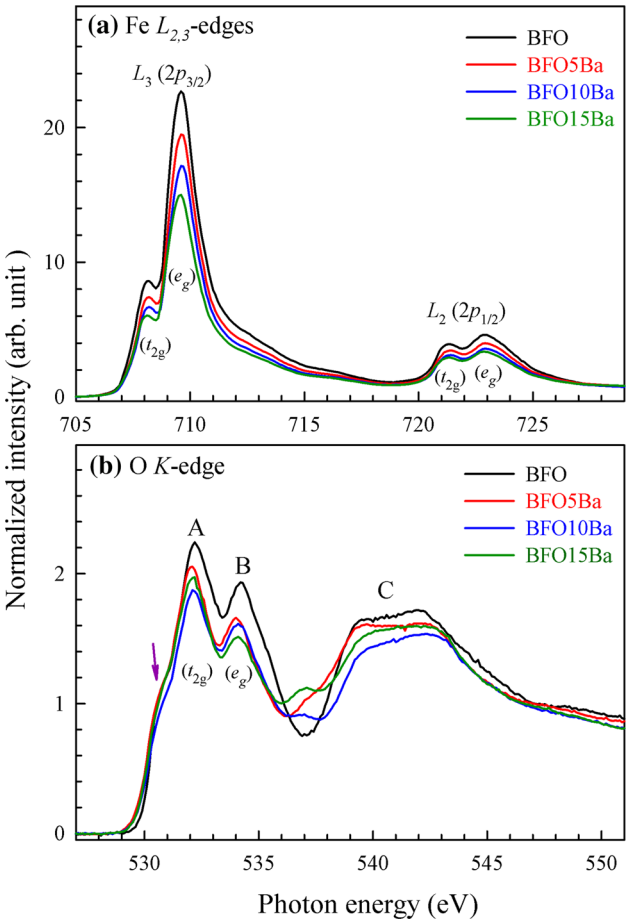

Figure 3 **a** Fe $L_{2,3}$-edge and **b** O *K*-edge X-ray absorption spectra versus photon energy.

loss of bismuth during the high-temperature synthesis. As discussed in the following paragraph, the synchrotron X-ray Fe *K*-edge absorption suggests an Fe^{3+} valence in all Ba-doped BFO compounds. The reduction of OVs in Ba-doped BFO compounds may correlate to possible higher binding energy in the Ba^{2+}–O bond compared with the Bi^{3+}–O bond in the perovskite $(Bi_{1-x}Ba_x)FeO_{3-\delta}$ as implied by the higher melting point in BaO than in Bi_2O_3 [51]. Thus, the loss of bismuth ions may be reduced by the A-site Ba^{2+} substitution. The XRD spectrum of BFO5Ba exhibits minor second phases of possible $Bi_2Fe_4O_9$ (or $Bi_{24}Fe_2O_{39}$/$Bi_{25}FeO_{39}$) as indicated by "*" in Fig. 1d, which were often observed in BFO ceramics prepared by solid-state synthesis [52–54]. The 2θ splitting of the XRD peaks decreases with increasing Ba substitution, suggesting a structural transition from low-symmetry rhombohedral to high-symmetry pseudocubic phase.

The Fe *K*-edge XAS spectra were measured as shown in Fig. 2a, including the reference powders FeO and Fe_2O_3. The Fe *K*-edge absorption arises primarily from the $1s \rightarrow 4p$ transition [55]. There is no obvious Fe *K*-edge energy shift in Ba-doped BFO compounds compared with Fe_2O_3, confirming an Fe^{3+} valence state. As indicated by the arrow, a weak pre-edge peak appears at ~7113 eV due to the $1s \rightarrow 3d$ quadrupole transition. Figure 2b shows the extended X-ray absorption fine structure (EXAFS) oscillations in k space and exhibit similar $k^2\chi(k)$ spectra, suggesting that the A-site Ba^{2+} substitution does not influence short-range structural ordering. Figure 2c shows the Fourier transforms of the EXAFS

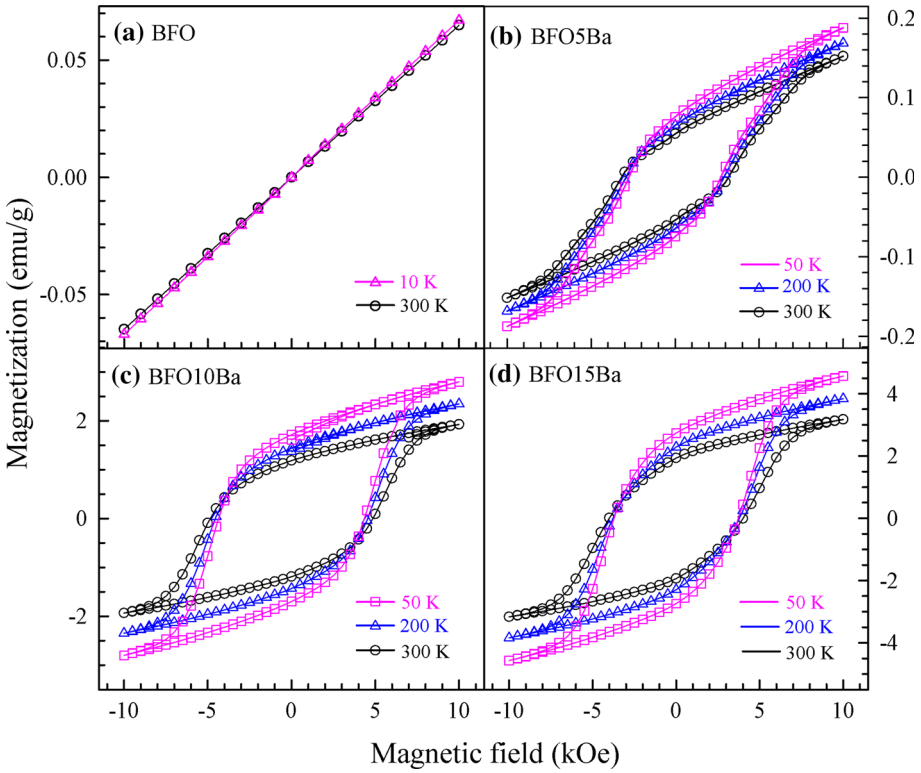

Figure 4 Hysteresis loops of magnetization versus magnetic field at and below room temperature.

$k^2\chi(k)$ spectra and the corresponding interatomic distances of Fe–O, Fe–Bi, and Fe–O–Fe bonds. The Fe–Bi and Fe–O–Fe bond lengths slightly increase and decrease, respectively, with increasing Ba substitution, suggesting a modulation of the Fe–O–Fe bond angle (where the two Fe^{3+} ions are in the centers of neighboring FeO_6 octahedra). The magnetic behavior of the Fe–O–Fe superexchange coupling is sensitive to bond angle and Fe 3*d* orbital states [56–58]. According to the Goodenough–Kanamori rules, the high-spin-state 180° $Fe^{3+}(t_{2g}^3e_g^2)$–O–Fe^{3+} $(t_{2g}^3e_g^2)$ superexchange interaction prefers an antiferromagnetic ordering [58, 59]. The Fe–O–Fe superexchange interaction shifts toward ferromagnetism as the Fe–O–Fe bond angle decreases toward 90° [56, 57].

Figure 3a shows the normalized Fe $L_{2,3}$-edge XAS spectra, corresponding to the transition from the Fe 2*p* core level to the unoccupied Fe 3*d* states [60]. The L_3 ($2p_{3/2}$) and L_2 ($2p_{1/2}$) bands appear in the regions of ~706–720 and ~720–728 eV, respectively. The splitting in the L_2 and L_3 bands is due to the 3*d* t_{2g} and e_g orbital states, as indicated in the brackets [61]. The $L_{2,3}$-edge profiles are similar to those for α-Fe_2O_3 [62, 63], confirming an Fe^{3+} valence as revealed in the Fe *K*-edge absorption in Fig. 2a. All compounds show similar $L_{2,3}$-edge profiles and peak energies, suggesting that A-site Ba^{2+} substitution does not significantly influence the Fe 3*d* states. Figure 3b shows the normalized O *K*-edge XAS from the O 1*s*→O 2*p* transition hybridized with the unoccupied Fe 3*d* orbitals [64, 65]. The A and B peaks are identified as t_{2g} and e_g bands due to the ligand-field splitting [66, 67], caused by the electrostatic interaction between the O 2*p* and the Fe 3*d* t_{2g} and e_g orbitals. Compared with BFO, the absorption peaks of the t_{2g} and e_g bands shift slightly toward lower energies in Ba-doped compounds. The peak intensity ratios of the A and B bands are about 2.25:1.94, 2.06:1.67, 1.89:1.62, and 1.98:1.51 for BFO, BFO5Ba, BFO10Ba, and BFO15Ba, respectively. The peak intensity ratio of the t_{2g} and e_g bands is associated with the Fe 3*d* hole number [64, 65]. Three t_{2g} and two e_g holes are in Fe $3d^5$ orbitals and thus a 3:2 ratio is expected in α-Fe_2O_3 without hybridization [65]. The O 2*p*–Fe 3*d* e_g hybridization is stronger than the O 2*p*–Fe 3*d* t_{2g} hybridization, thus a 1:1 ratio could experimentally occur in α-Fe_2O_3 [65]. As suggested by Groot et al. [64], the splitting of the *d* orbitals (t_{2g}, e_g) can be complex due to other mechanisms, such as electronic

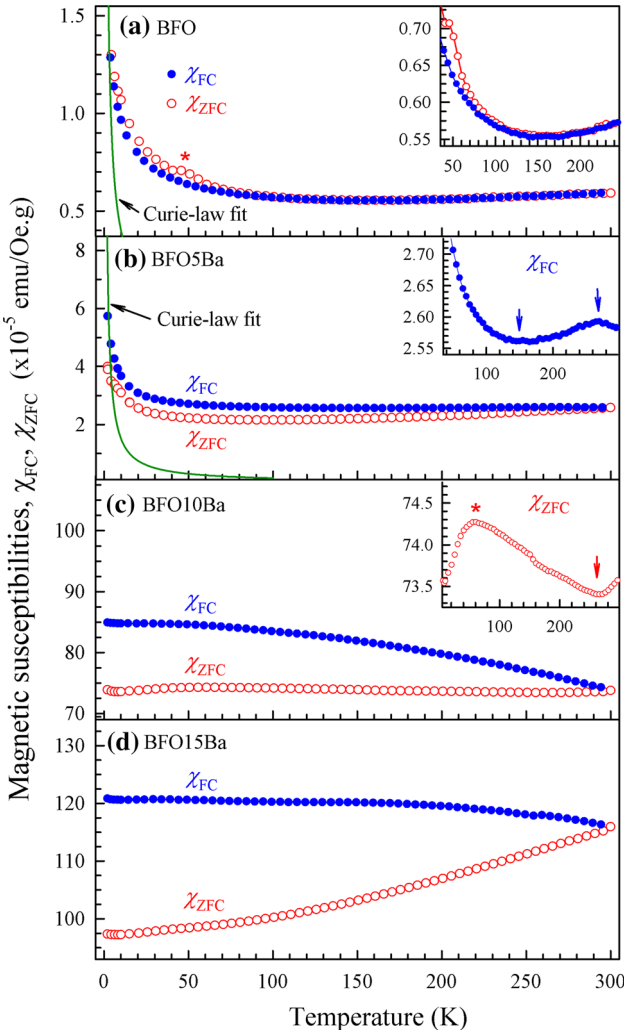

Figure 5 Zero-field-cooled and field-cooled magnetic susceptibilities (χ_{ZFC} and χ_{FC}) measured under a dc magnetic field (H = 100 Oe).

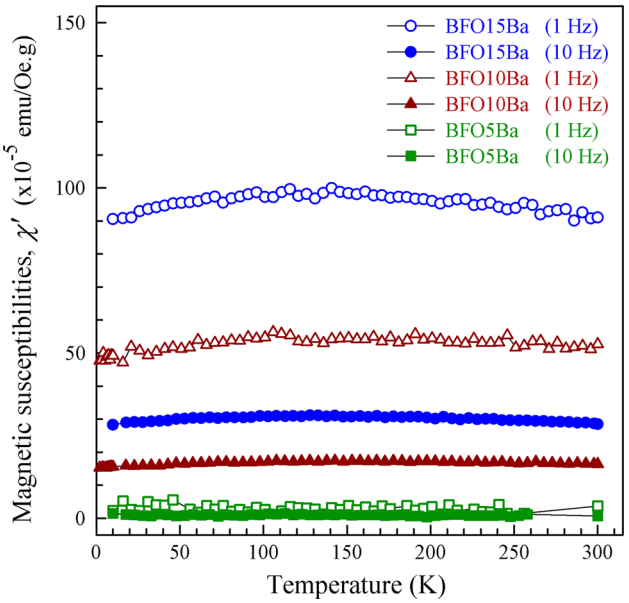

Figure 6 Real part (χ) of ac magnetic susceptibility for measuring frequencies $f = 1$ and 10 Hz.

exchange interactions and the non-stoichiometry effect [64]. The peak intensity ratios of A and B peaks in Fig. 3b show a slight increase in Ba-doped compounds, suggesting that the hybridization effect of the O 2*p* and Fe 3*d* orbitals was decreased by the A-site Ba substitution. The broad C band in the region of ~537–550 eV can be attributed to the mixture of Bi 6*p*, Ba 6*s*, Fe 4*s*/4*p*, and O 2*p* configurations [65, 68]. As indicated by the arrow, a weak pre-edge peak appears at ~530.5 eV and is attributed to the dipole transition from O 1*s* to the high-spin O 2*p* states hybridized with the unoccupied high-spin Fe $3d^5$ ($t_{2g}^3 e_g^2$) state [67, 68].

Figure 4 shows hysteresis loops of magnetization (M) versus magnetic field (H) at and below room temperature. BFO remains in a linear antiferromagnetic phase at 10 K. Ba-doped BFO compounds exhibit ferromagnetic hysteresis loops with increasing magnetization as Ba substitution increases. Ba-doped BFO compounds show weakly temperature-dependent coercive fields with increasing ferromagnetic magnetization as temperature decreases below room temperature. First-principles density functional theory suggests that a ferromagnetic magnetization may develop in BFO under oxygen-rich sintering conditions [69]. The enhanced ferromagnetic magnetization in Ba-doped BFO compounds may correlate to fewer OVs as shown in Fig. 1 and the modulation of the Fe–O–Fe bond angle as shown in Fig. 2c.

Figure 5 shows dc ZFC and FC magnetic susceptibilities (χ_{ZFC} and χ_{FC}). χ_{ZFC} and χ_{FC} increase as Ba substitution increases and are consistent with the enhanced magnetizations shown in Fig. 4. As shown in Fig. 5a for BFO, a minor splitting between χ_{ZFC} and χ_{FC} begins at ~150 K, suggesting a weak spin-glass transition [26–28, 70]. This magnetization irreversibility is mainly due to the magnetic anisotropy and competing magnetic interactions (or orderings) [30]. χ_{ZFC} and χ_{FC} decrease with decreasing temperature down to ~150 K accompanied by a weak minimum (as enlarged in the inset) and then increase with further decrease of temperature. This indicates

an onset of paramagnetic behavior below ~150 K possibly due to paramagnetic impurities. The solid line is the Curie law fit to estimate the paramagnetic contribution below 10 K, i.e., $\chi_P = C/T$ [71], with the Curie constant $C = 4\times10^{-5} K{\cdot}emu/Oe{\cdot}g$. The appearance of paramagnetic ordering in the antiferromagnetic matrix can result in magnetic frustration and thus cause spin-glass splitting. χ_{ZFC} shows a weak cusp at ~50 K (as indicated by the asterisk), which is similar to the ZFC magnetization cusp at ~50 K in bulk BFO [70]. This ZFC susceptibility anomaly was attributed to domain-wall pinning effects as a result of structural distortions [70, 72]. A similar but stronger ZFC magnetization cusp was seen in γ-Fe_2O_3 nanoparticles at the blocking temperature T_B ~ 72 K [73].

In BFO5Ba, χ_{FC} exhibits a local maximum at ~260 K as shown in the inset of Fig. 5b, suggesting a minor transition of magnetic ordering in the weak

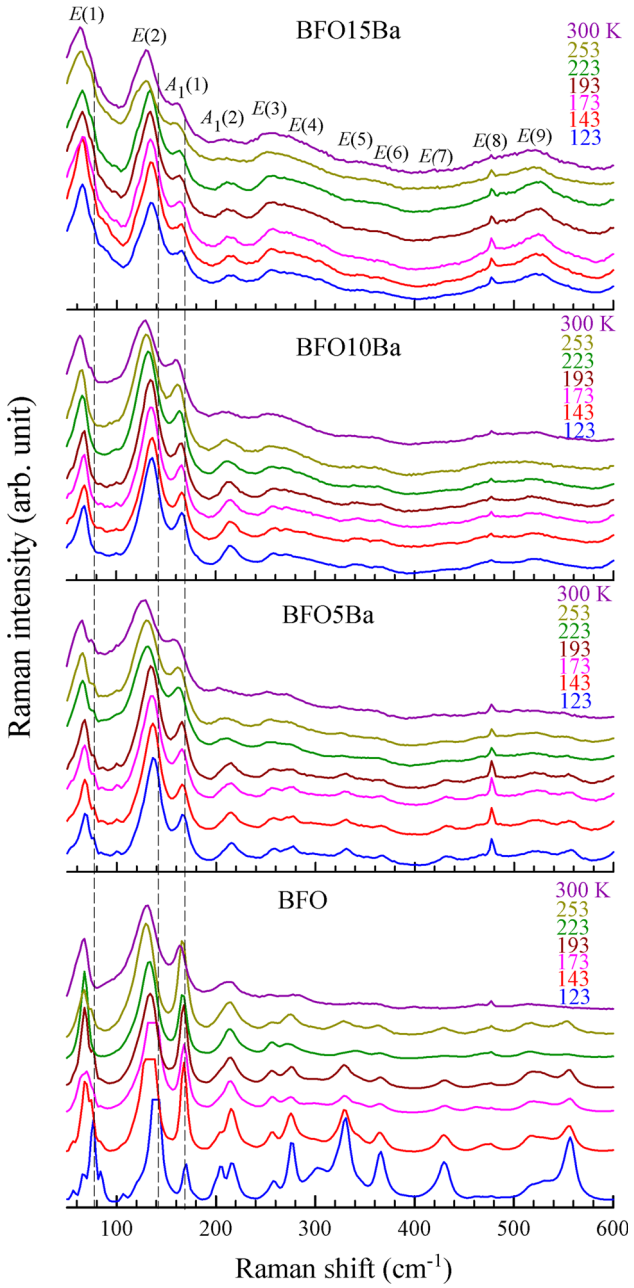

Figure 7 Temperature-dependent Raman spectra of BFO, BFO5Ba, BFO10Ba, and BFO15Ba.

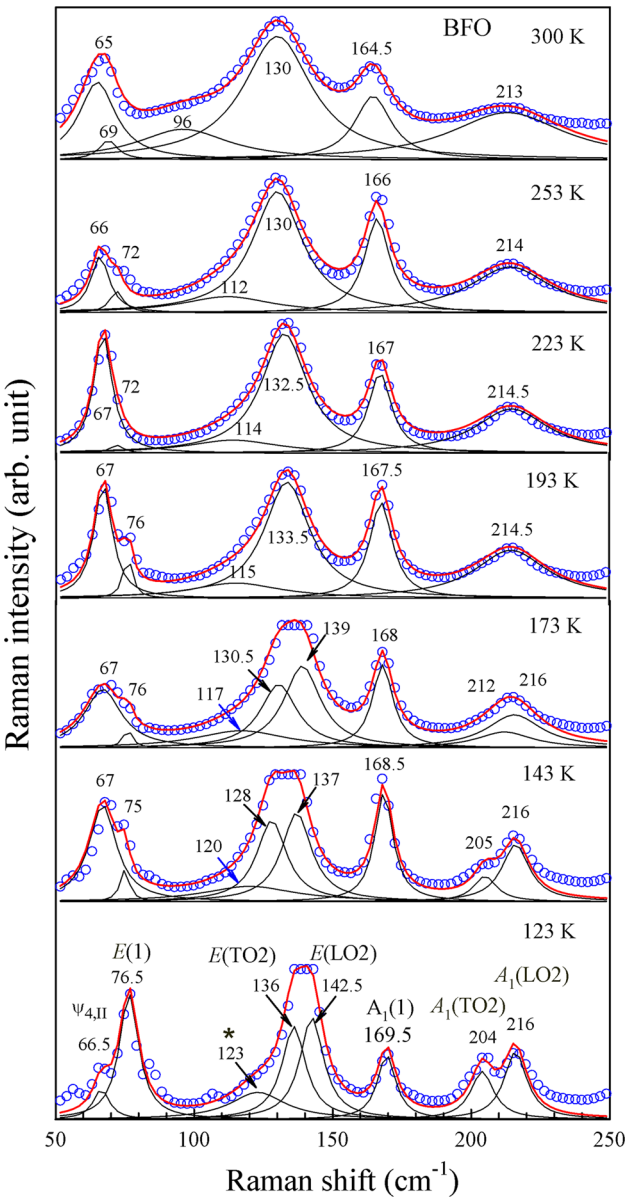

Figure 8 Raman spectra (50–250 cm^{-1}) and Lorentzian function fits for BFO. The *red lines* are the sums of fitting modes. The labeled numbers are frequencies of Raman modes.

ferromagnetic matrix. Both χ_{ZFC} and χ_{FC} increase as the temperature decreases below ~150 K, indicating a paramagnetic contribution due to paramagnetic impurities as observed in BFO. The solid line in Fig. 5b is the Curie law fit with $C = 1.5 \times 10^{-4}$ *K·emu/Oe·g*. The spin-glass splitting in BFO5Ba below room temperature is likely associated with the appearance of paramagnetic ordering in the weak ferromagnetic matrix. Figure 6 shows temperature-dependent ac magnetic susceptibilities (χ') for measuring frequencies $f = 1$ and 10 Hz. BFO5Ba exhibits a weak frequency-dependent ac magnetic susceptibility (χ'), suggesting a weak spin-glass phase.

In Fig. 5c, χ_{FC} in BFO10Ba exhibits a gradual increase with the decrease of temperature. This is consistent with a gradual increase in magnetization as shown in Fig. 4c. χ_{ZFC} exhibits a local minimum at ~260 K as shown in the inset of Fig. 5c, suggesting a weak magnetic ordering transition. A broad local maximum at ~60 K (as indicated by the asterisk in the inset) appears in the ZFC curve and is similar to the ZFC magnetization cusp near 50 K in bulk BFO [70]. In Fig. 5d, BFO15Ba exhibits a weakly temperature-dependent χ_{FC} accompanied with a broad maximum near 150 K in the real part χ' of as susceptibility in Fig. 6, suggesting a magnetic ordering transition. The spin-glass splitting in BFO10Ba and NFO15Ba is likely associated with the competition of various magnetic orderings in the ferromagnetic matrix, which can result in local magnetic anisotropy (or frustration). BFO10Ba and BFO15Ba exhibit strong frequency-dependent broad maxima in ac susceptibilities (χ') as shown in Fig. 6, revealing a spin-glass phase.

Figure 7 shows Raman-active modes in the frequency range of 50–600 cm^{-1} as the temperature increases in steps. The *R*3c rhombohedral $BiFeO_3$ unit cell contains two formula units ($Z = 2$) and has 13 Raman-active modes, i.e., $4A_1 + 9E$ [74–76]. Four major modes appear below 250 cm^{-1}: $E(1)$ (~60–80 cm^{-1}), $E(2)$ (~130–140 cm^{-1}), $A_1(1)$ (~160–170 cm^{-1}), and $A_1(2)$ (~210–220 cm^{-1}) [74]. Vibrational frequencies corresponding to Bi, Fe, and O atoms mainly appear below ~170 cm^{-1}, between ~150 and ~270 cm^{-1}, and above ~260 cm^{-1}, respectively [74]. As illustrated by the dashed lines, the $E(1)$, $E(2)$, $A_1(1)$, and $A_1(2)$ modes shift toward lower frequencies as the temperature increases. The increasing broadness in full-width-at-half-maxima (FWHMs) upon heating is mainly associated with thermally excited dynamic effects due to lattice fluctuations.

Figures 8, 9, 10, and 11 show temperature-dependent Raman modes in the frequency range of 50–250 cm^{-1}. The Raman modes were fitted using the Lorentzian function as shown by black solid curves with frequencies labeled on the top of the peaks. The Raman mode at 63–67 cm^{-1} (123 K) was assigned to the first overtone ($\psi_{4,II}$) of the magnon mode ψ_4 (~32–33 cm^{-1}) [47]. The relatively broad Raman modes in the region of 90–120 cm^{-1} (as

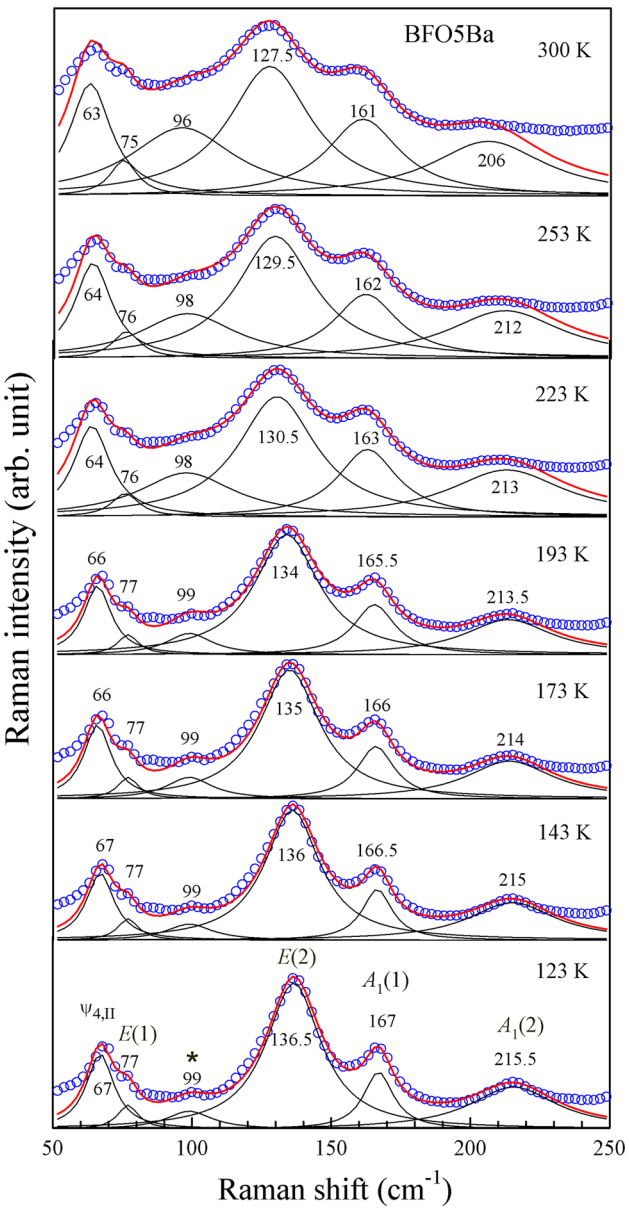

Figure 9 Raman spectra and Lorentzian function fits for BFO5Ba.

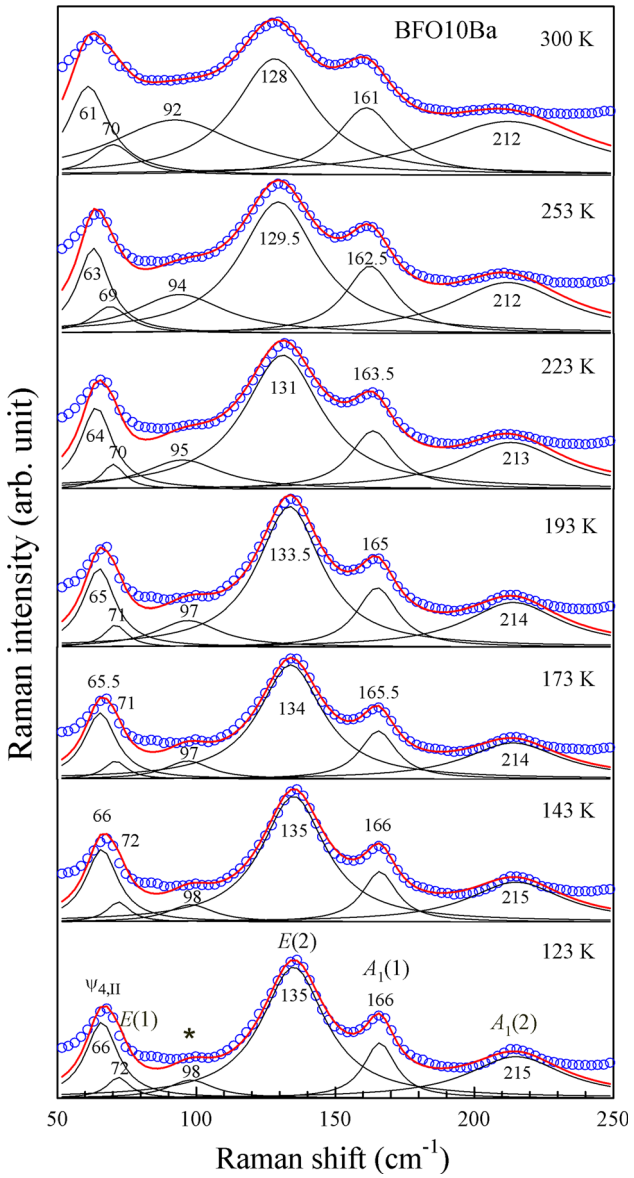

Figure 10 Raman spectra and Lorentzian function fits for BFO10Ba.

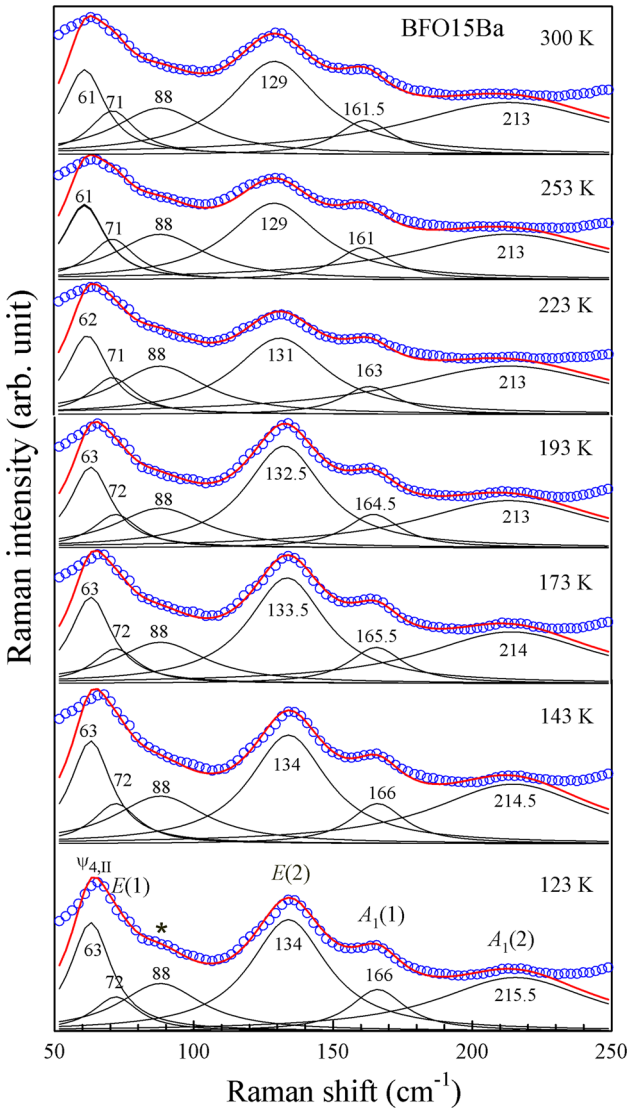

Figure 11 Raman spectra and Lorentzian function fits for BFO15Ba.

indicated by "*") are likely overtones of low-lying magnons, which were observed below 60 cm^{-1} [47]. The $E(2)$ mode of BFO exhibits a broad plateau below ~170 K, revealing a combination of E(TO2) and E(LO2) modes. "LO" and "TO" represent longitudinal and transverse optical modes, respectively. The $A_1(2)$ mode of BFO shows clear splitting of A_1(LO2) and A_1(TO2) modes with $\Delta\omega$ ~10 cm^{-1} below ~173 K. The A_1 modes in the $R3c$ symmetry constitute vibrations along the $[111]_C$ polarization direction [40, 44]. The $A_1(1)$ and $A_1(2)$ modes are mainly associated with Fe atom motion [74] and thus are sensitive to vibrations of the Fe–O–Fe bond. The $E(1)$ and $E(2)$ vibrational frequencies are mainly associated with Bi atom motion [74] and are sensitive to A-site Ba substitution. Hence, the A_1 and E modes are sensitive to the coupling between Fe $3d$ spin and phonon.

Temperature-dependent Raman frequencies and FWHMs of the $\psi_{4,II}$, $E(2)$, and $A_1(1)$ modes are plotted in Figs. 12 and 13. In BFO, the E(LO2) and E(TO2) modes merge into a single peak near ~170 K. This

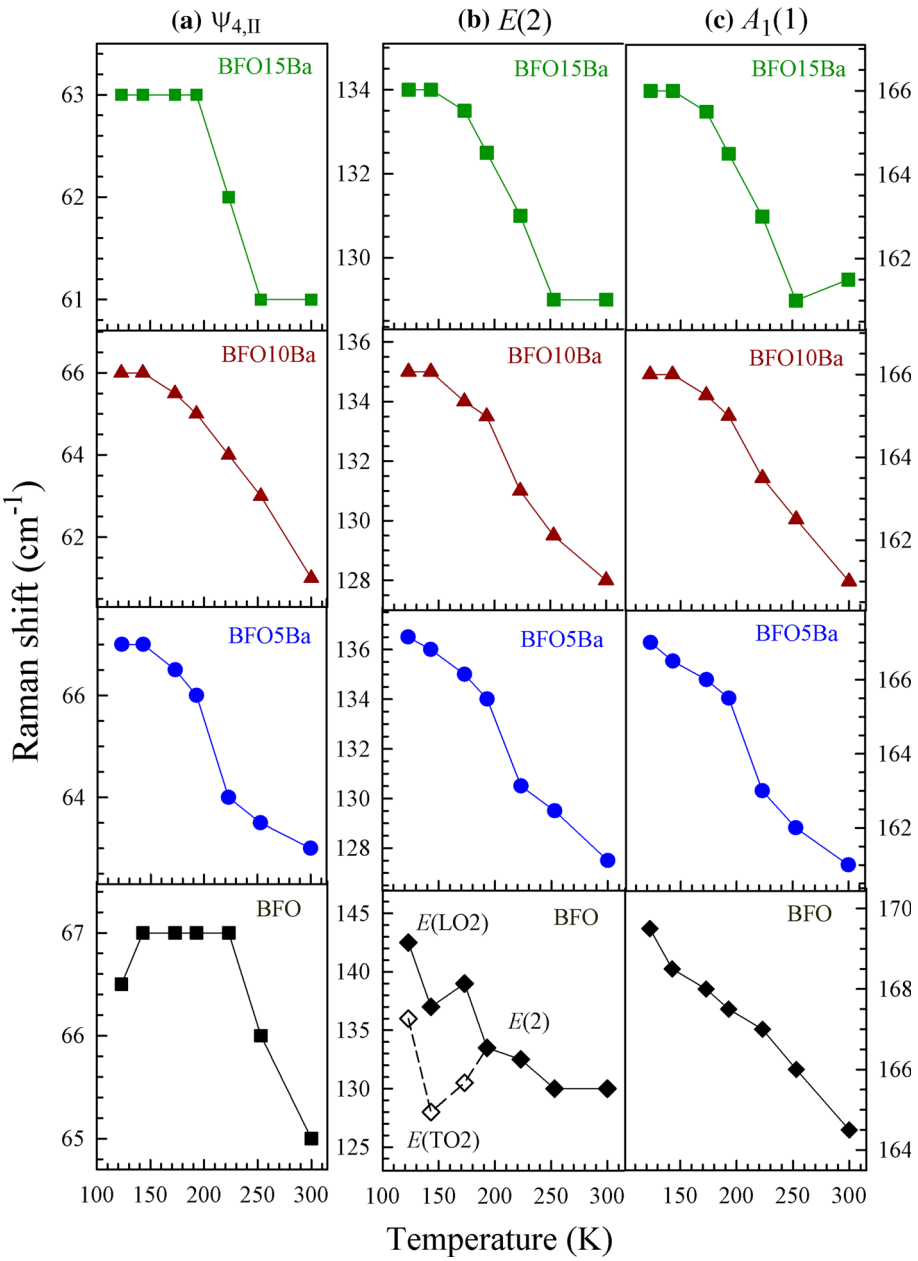

Figure 12 Temperature-dependent Raman shifts of the $\psi_{4,II}$, $E(2)$, and $A_1(1)$ modes.

phonon splitting may result from the spin–phonon coupling, while the weak spin-glass transition occurs below ~150 K as observed in Fig. 5a. The $\psi_{4,II}$, $E(2)$, and $A_1(1)$ modes in BFO5Ba and BFO10Ba exhibit softening anomalies over a wide frequency range in the temperature region of ~150–250 K upon heating. As shown in Fig. 12, BFO15Ba exhibits step-like anomalies in frequency shifts of the $\psi_{4,II}$, $E(2)$, and $A_1(1)$ modes with an onset at ~150–200 K. This strong phonon effect may be associated with the anomaly at ~150 K in χ_{FC}, as shown in Fig. 5d. As seen in Fig. 13, FWHMs of the $E(2)$ and $A_1(1)$ modes in BFO, BFO5Ba, and BFO10Ba increase significantly as the temperature increases. The $E(2)$ modes of BFO10Ba and BFO15Ba exhibit a step-like anomaly in FWHMs at around 200 K. Neutron scattering reported broad phonon modes in polycrystalline $BiFeO_3$ with increasing temperature, corresponding to the phonon damping and spin–phonon coupling [77]. χ_{ZFC} and χ_{FC} in Fig. 5 suggest a magnetic ordering transition at ~150 K in BFO5Ba and BFO15Ba and at ~260 K in BFO10Ba. The phonon anomalies in the Bi- and Fe-sensitive $E(2)$ and $A_1(1)$ modes at ~150–250 K likely result from the spin–phonon

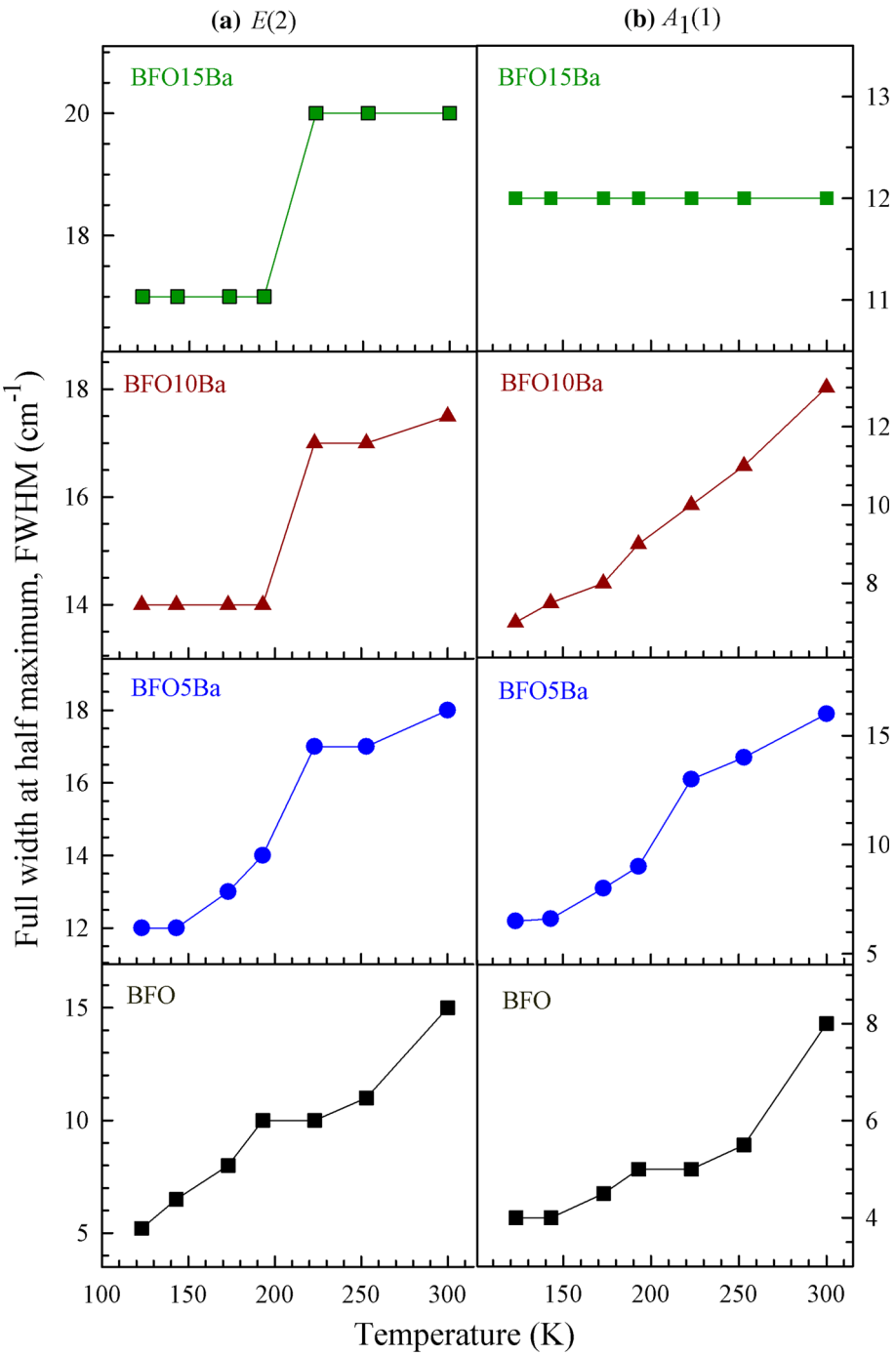

Figure 13 Temperature-dependent FWHMs of the $E(2)$ and $A_1(1)$ modes.

interaction while magnetic ordering transitions take place.

Conclusions

Ba-doped BFO compounds show ferromagnetism with increasing magnetization as Ba^{2+} substitution increases. The enhanced ferromagnetic magnetizations in Ba-doped BFO compounds are attributed to fewer oxygen vacancies (OVs) and the modulation of the Fe–O–Fe bond angle, as revealed by the synchrotron XAS. The oxygen *K*-edge XAS suggests a reduction of hybridization of the O 2*p* and Fe 3*d* orbitals by Ba substitution. The dc (χ_{ZFC} and χ_{FC}) and ac (χ') magnetic susceptibilities reveal an enhanced spin-glass behavior in Ba-doped BFO compounds, which is attributed to the competition of

various magnetic orderings in the ferromagnetic matrix. The Bi- and Fe-sensitive $E(2)$ and $A_1(1)$ phonon modes reveal significant frequency softening and step-like anomalies in FWHM in the vicinity of ~150–250 K, which likely result from the spin–phonon interaction.

Acknowledgements

This project is supported by the Ministry of Science and Technology of Taiwan (MOST) under Project Nos. 104-2221-E-030-014 and 104-2221-E-146-001.

Compliance with ethical standards

Conflict of Interest The authors declare that they have no conflict of interest.

References

[1] Sando D, Agbelele A, Rahmedov D et al (2013) Crafting the magnonic and spintronic response of $BiFeO_3$ films by epitaxial strain. Nat Mater 12:641–646

[2] Kumar A, Scott JF, Katiyar RS (2011) Electric control of magnon frequencies and magnetic moment of bismuth ferrite thin films at room temperature. Appl Phys Lett 99:062504

[3] Bhide VG, Multani MS (1965) Mössbauer effect in ferroelectric-antiferromagnetic $BiFeO_3$. Solid State Commun 3:271–274

[4] Ravindran P, Vidya R, Kjekshus A et al (2006) Theoretical investigation of magnetoelectric behavior in $BiFeO_3$. Phys Rev B 74:224412

[5] Sosnowska I, Peterlin-Neumaier T, Steichele E (1982) Spiral magnetic ordering in bismuth ferrite. J Phys C 15:4835–4846

[6] Sosnowska IM (2009) Neutron scattering studies of $BiFeO_3$ multiferroics: a review for microscopists. J Microsc 236: 109–114

[7] Przeniosło R, Palewicz A, Regulski M et al (2006) Does the modulated magnetic structure of $BiFeO_3$ change at low temperatures? J Phys 18:2069–2075

[8] Arnold DC (2015) Composition-driven structural phase transitions in rare-earth-doped $BiFeO_3$ ceramics: a review. IEEE Trans Ultrason, Ferroelect, Freq Control 62:62–82

[9] Chang LY, Tu CS, Chen PY et al (2016) Raman vibrations and photovoltaic conversion in rare earth doped $(Bi_{0.93}R_{0.07})FeO_3$ (R = Dy, Gd, Eu, Sm) ceramics. Ceram Int 42:834–842

[10] Tu CS, Chen CS, Chen PY et al (2016) Raman vibrations, domain structures and photovoltaic effects in A-site La-modified $BiFeO_3$ multiferroic ceramics. J Am Ceram Soc 99:674–681

[11] Tu CS, Chen CS, Chen PY et al (2016) Enhanced photovoltaic effects in A-site samarium doped $BiFeO_3$ ceramics: the roles of domain structure and electronic state. J Eur Ceram Soc 36:1149–1157

[12] Gautam A, Rangra VS (2010) Effect of Ba ions substitution on multiferroic properties of $BiFeO_3$ perovskite. Cryst Res Technol 45:953–956

[13] Khomchenko VA, Kiselev DA, Vieira JM et al (2008) M. Maglione, Effect of diamagnetic Ca, Sr, Pb, and Ba substitution on the crystal structure and multiferroic properties of the $BiFeO_3$ perovskite. J Appl Phys 103:024105

[14] Wang DH, Goh WC, Ming M et al (2006) Effect of Ba doping on magnetic, ferroelectric, and magnetoelectric properties in multiferroic $BiFeO_3$ at room temperature. Appl Phys Lett 88:212907

[15] Li P, Lin YH, Nan CW (2011) Effect of nonmagnetic alkaline-earth dopants on magnetic properties of $BiFeO_3$ thin films. J Appl Phys 110:033922

[16] Das R, Mandal K (2012) Magnetic, ferroelectric and magnetoelectric properties of Ba-doped $BiFeO_3$. J Magn Magn Mater 324:1913–1918

[17] Chang HW, Shen CY, Yuan FT et al (2015) Multiferroic properties of (Bi, Ca)FeO3 films on glass substrates. Appl Surf Sci 355:121–126

[18] Tu CS, Xu ZR, Schmidt VH et al (2015) A-site strontium doping effects on structure, magnetic, and photovoltaic properties of $(Bi_{1-x}Sr_x)FeO_3$ multiferroic ceramics. Ceram Int 41:8417–8424

[19] Chang HW, Yuan FT, Tu KT et al (2015) Effect of Ba substitution on the multiferroic properties of $BiFeO_3$ films on glass substrates. J Appl Phys 117:17C734

[20] Hung CM, Tu CS, Xu ZR et al (2014) Effect of diamagnetic barium substitution on magnetic and photovoltaic properties in multiferroic $BiFeO_3$. J Appl Phys 115:17D901

[21] Xu ZR, Tu CS, Hung CM et al (2014) Magnetic and photovoltaic properties of calcium-doped $BiFeO_3$ ceramic. IEEE Trans Magn 50:2500304

[22] Rangi M, Agarwal A, Sanghi S et al (2014) Crystal structure and magnetic properties of $Bi_{0.8}A_{0.2}FeO_3$ (A = La, Ca, Sr, Ba) multiferroics using neutron diffraction and Mossbauer spectroscopy. AIP Adv 4:087121

[23] Khomchenko VA, Kopcewicz M, Lopes AML et al (2008) Intrinsic nature of the magnetization enhancement in heterovalently doped $Bi_{1-x}A_xFeO_3$ (A = Ca, Sr, Pb, Ba) multiferroics. J Phys D Appl Phys 41:102003

[24] Das R, Sharma S, Mandal K (2016) Aliovalent Ba^{2+} doping: a way to reduce oxygen vacancy in multiferroic $BiFeO_3$. J Magn Magn Mater 401:129–137

[25] Makhdoom AR, Akhtar MJ, Rafiq MA et al (2012) Investigation of transport behavior in Ba doped $BiFeO_3$. Ceram Int 38:3829–3834
[26] Singh MK, Prellier W, Singh MP et al (2008) Spin-glass transition in single-crystal $BiFeO_3$. Phys Rev B 77:144403
[27] Gaikwad VM, Acharya SA (2014) Investigation on magnetic behaviour of $BiFeO_3$: SPIN glass view point. Adv Mat Lett 5:157–160
[28] Singh MK, Katiyar RS, Prellier W et al (2009) The Almeida-Thouless line in BiFeO3: is bismuth ferrite a mean field spin glass? J Phys 21:042202
[29] Singh MK, Prellier W, Jang HM et al (2009) Anomalous magnetic ordering induced spin phonon coupling in $BiFeO_3$ thin films. Solid State Commun 149:1971–1973
[30] Joyy PA, Kumarz PSA, Date SK (1998) The relationship between field-cooled and zero-field-cooled susceptibilities of some ordered magnetic systems. J Phys 10:11049–11054
[31] Koshizuka N, Ushioda S (1980) Inelastic-light-scattering study of magnon softening in $ErFeO_3$. Phys Rev B 22:5394–5399
[32] Venugopalan S, Dutta M, Ramdas AK et al (1983) Raman scattering study of magnons at the spin-reorientation transitions of $TbFeO_3$ and $TmFeO_3$. Phys Rev B 27:3115–3118
[33] Litvinchuk AP, Iliev MN, Popov VN et al (2004) Raman and infrared-active phonons in hexagonal $HoMnO_3$ single crystals: magnetic ordering effects. J Phys 16:809–819
[34] Sharma PA, Ahn JS, Hur N et al (2004) Thermal conductivity of geometrically frustrated, ferroelectric $YMnO_3$: extraordinary spin-phonon interactions. Phys Rev Lett 93:177202
[35] Yamaguchi T (1974) Theory of spin reorientation in rare-earth orthochromites and orthoferrites. J Phys Chem Solids 35:479–500
[36] Catalan G, Scott JF (2009) Physics and applications of bismuth ferrite. Adv Mater 21:2463–2485
[37] Fukumura H, Matsui S, Harima H et al (2007) Observation of phonons in multiferroic $BiFeO_3$ single crystals by Raman scattering. J Phys 19:365224
[38] Singh MK, Katiyar RS, Scott JF (2008) New magnetic phase transitions in $BiFeO_3$. J Phys 20:252203
[39] Palai R, Schmid H, Scott JF et al (2010) Raman spectroscopy of single-domain multiferroic $BiFeO_3$. Phys Rev B 81:064110
[40] Beekman C, Reijnders AA, Oh YS et al (2012) Raman study of the phonon symmetries in $BiFeO_3$ single crystals. Phys Rev B 86:020403
[41] Kothari D, Reddy VR, Sathe VG et al (2008) Raman scattering study of polycrystalline magnetoelectric $BiFeO_3$. J Magn Magn Mater 320:548–552
[42] Rout D, Moon KS, Kang SJL (2009) Temperature-dependent Raman scattering studies of polycrystalline $BiFeO_3$ bulk ceramics. J Raman Spectrosc 40:618–626
[43] Kumar A, Scott JF, Katiyar RS (2012) Magnon Raman spectroscopy and in-plane dielectric response in $BiFeO_3$: relation to the Polomska transition. Phys Rev B 85:224410
[44] Iliev MN, Abrashev MV, Mazumdar D et al (2010) Polarized Raman spectroscopy of nearly tetragonal $BiFeO_3$ thin films. Phys Rev B 82:014107
[45] Khabiri G, Anokhin AS, Razumnaya AG et al (2014) Phonon and magnon excitations in Raman spectra of an epitaxial bismuth ferrite film. Phys Solid State 56:2507–2513
[46] Palai R, Scott JF, Katiyar RS (2010) Phonon spectroscopy near phase transition temperatures in multiferroic $BiFeO_3$ epitaxial thin films. Phys Rev B 81:024115
[47] Cazayous M, Gallais Y, Sacuto A et al (2008) Possible observation of cycloidal electromagnons in $BiFeO_3$. Phys Rev Lett 101:037601
[48] Herrero-Albillos J, Catalan G, Rodriguez-Velamazan JA et al (2010) Neutron diffraction study of the $BiFeO_3$ spin cycloid at low temperature. J Phys 22:26001
[49] Ramazanoglu M, Ratcliff W, Choi YJ et al (2011) Temperature-dependent properties of the magnetic order in single-crystal $BiFeO_3$. Phys Rev B 83:174434
[50] Jeong J, Le MD, Bourges P et al (2014) Temperature-dependent interplay of Dzyaloshinskii-Moriya interaction and single-ion anisotropy in multiferroic $BiFeO_3$. Phys Rev Lett 113:107202
[51] Barin I, Knacke O (1973) Thermochemical properties of inorganic substances. Springer, New York, pp 77–112
[52] Lahmar A, Zhao K, Habouti S et al (2011) Off-stoichiometry effects on $BiFeO_3$ thin films. Solid State Ionics 202:1–5
[53] Karimi S, Reaney IM, Han Y et al (2009) Crystal chemistry and domain structure of rare-earth doped $BiFeO_3$ ceramics. J Mater Sci 44:5102–5112. doi:10.1007/s10853-009-3545-1
[54] Lufaso MW, Vanderach TA, Pazos M et al (2006) Phase formation, crystal chemistry, and properties in the system Bi_2O_3–Fe_2O_3–Nb_2O_5. J Solid State Chem 179:3900–3910
[55] Grunes LA (1983) Study of the K edges of 3d transition metals in pure and oxide form by X-ray-absorption spectroscopy. Phys Rev B 27:2111–2131
[56] Anderson PW (1950) Antiferromagnetism theory of superexchange interaction. Phys Rev 79:350–356
[57] Ota N (2014) Super-exchange ferromagnetic order analysis of FeO-modified graphene-snano-ribbon. J Magn Soc Jpn 38:107–110
[58] Goodenough JB (1963) Magnetism and the chemical bond. Wiley, New York, pp 174–178

[59] Bi L, Taussig AR, Kim HS et al (2008) Structural, magnetic, and optical properties of $BiFeO_3$ and Bi_2FeMnO_6 epitaxial thin films: an experimental and first-principles study. Phys Rev B 78:104106

[60] Higuchi T, Sakamoto W, Itoh N et al (2008) Valence state of Mn-doped $BiFeO_3$-$BaTiO_3$ ceramics probed by soft X-ray absorption spectroscopy. Appl Phys Exp 1:011502

[61] Ikeno H, Tanaka I, Miyamae T et al (2004) First principles calculation of Fe $L_{2,3}$-edge X-ray absorption near edge structures of iron oxides. Mater Trans 45:1414–1418

[62] Miedema PS, Groot FMF (2013) The iron L edges: Fe 2p X-ray absorption and electron energy loss spectroscopy. J Electron Spectrosc Relat Phenom 187:32–48

[63] Crocombette JP, Pollak M, Joliet F et al (1995) X-ray-absorption spectroscopy at the Fe $L_{2,3}$ threshold in iron oxides. Phys Rev B 52:3143–3150

[64] de Groot FMF, Gnom M, Fuggle JC (1989) Oxygen 1 s x-ray-absorption edges of transition-metal oxides. Phys Rev B 40:5715–5723

[65] Wu ZY, Gota S, Jollet F et al (1997) Characterization of iron oxides by x-ray absorption at the oxygen *K* edge using a full multiple-scattering approach. Phys Rev B 55:2570–2577

[66] Ma Y, Johnson PD, Wassdahl N et al (1993) Electronic structures of α-Fe_2O_3 and Fe_3O_4 from O *K*-edge absorption and emission spectroscopy. Phys Rev B 48:2109–2111

[67] Ballhausen CJ (1962) Introduction to ligand-field theory. McGraw-Hill, New York

[68] Douma DH, Ciprian R, Lamperti A et al (2014) Experimental versus ab initio x-ray absorption of iron-doped zirconia: trends in O *K*-edge spectra as a function of iron doping. Phys Rev B 90:205201

[69] Paudel TR, Jaswal SS, Tsymbal EY (2012) Intrinsic defects in multiferroic $BiFeO_3$ and their effect on magnetism. Phys Rev B 85:104409

[70] Park TJ, Papaefthymiou GC, Viescas AJ et al (2007) Size-dependent magnetic properties of single-crystalline multiferroic $BiFeO_3$ nanoparticles. Nano Lett 7:766–772

[71] Spaldin NA (2011) Magnetic Materials, 2nd edn. Cambridge, New York

[72] Sankar CR, Joy PA (2005) Magnetic properties of the self-doped lanthanum manganites $La_{1-x}MnO_3$. Phys Rev B 72:024405

[73] Martínez B, Obradors X, Balcells L et al (1998) Low temperature surface spin-glass transition in γ-Fe_2O_3 nanoparticles. Phys Rev Lett 80:181–184

[74] Hermet P, Gofinet M, Kreisel J et al (2007) Raman and infrared spectra of multiferroic bismuth ferrite from first principles. Phys Rev B 75:220102

[75] Hlinka J, Pokorny J, Karimi S et al (2011) Angular dispersion of oblique phonon modes in $BiFeO_3$ from micro-Raman scattering. Phys Rev B 83:020101

[76] Bielecki J, Svedlindh P, Tibebu DT et al (2012) Structural and magnetic properties of isovalently substituted multiferroic $BiFeO_3$: insights from Raman spectroscopy. Phys Rev B 86:184422

[77] Delaire O, Stone MB, Ma J et al (2012) Anharmonic phonons and magnons in $BiFeO_3$. Phys Rev B 85:064405